

Radio Activity from the Rapidly Rotating T dwarf 2MASS 2228-4310

Kelvin Wandia,¹* Michael A. Garrett,^{1,2} Aaron Golden,³ Gregg Hallinan,⁴ David Williams-Baldwin,¹ Geferson Lucatelli,¹ Robert J. Beswick,¹ Jack F. Radcliffe,^{1,5} Andrew Siemion,^{1,6,7,8,9,10,11}

Talon Myburgh¹²

¹Jodrell Bank Centre for Astrophysics (JBCA), Department of Physics & Astronomy, Alan Turing Building, The University of Manchester, M13 9PL, UK

²Leiden Observatory, Leiden University, PO Box 9513, 2300 RA Leiden, The Netherlands

³Physics, School of Natural Sciences & Center for Astronomy, College of Science and Engineering, University of Galway, University Road, Galway, H91 TK33, Ireland

⁴Division of Physics, Mathematics, and Astronomy, California Institute of Technology, Pasadena, CA 91125, USA

⁵Department of Physics, University of Pretoria, Lynnwood Road, Hatfield, Pretoria, 0083, South Africa

⁶SETI Institute, 339 Bernardo Ave, Suite 200, Mountain View, CA 94043, USA

⁷Berkeley SETI Research Center, University of California, Berkeley, CA 94720, USA

⁸Breakthrough Listen, Astrophysics, Department of Physics, The University of Oxford, Keble Road, Oxford, OX1 3RH, UK

⁹Astrophysics, Department of Physics, University of Oxford, Keble Road, Oxford, OX1 3RH, UK

¹⁰Berkeley SETI Research Center, University of California, Berkeley, CA 94720, USA

¹¹University of Malta, Institute of Space Sciences and Astronomy, Msida, MSD2080, Malta

¹²Centre for Radio Astronomy Techniques and Technologies, Department of Physics and Electronics, Rhodes University, Makhanda, 6140, South Africa

Accepted XXX. Received YYY; in original form ZZZ

ABSTRACT

We present the detection of 2MASS J22282889-4310262 (2M2228), a T6/T6.5 brown dwarf, using the Karl G. Jansky Very Large Array (VLA) archival data observed at C band (4–8 GHz) over two observing epochs (2×96 minutes). 2M2228 is detected at time and frequency averaged Stokes I and V peak flux densities of $67.3 \pm 4.9 \mu\text{Jy beam}^{-1}$ and $14.4 \pm 3.0 \mu\text{Jy beam}^{-1}$ in the first epoch and $107.2 \pm 5.2 \mu\text{Jy beam}^{-1}$ and $-20.7 \pm 1.2 \mu\text{Jy beam}^{-1}$ in the second epoch. This discovery constitutes the eighth and, notably, the most rapidly rotating T dwarf detected to date at radio wavelengths. Our observations reveal highly polarised bursts at fractional polarisation ratios $f_c > 50\%$. Using Stokes I light curves, we measure occurrence intervals of ~ 47 and ~ 58 minutes in the two observing epochs respectively with the first burst aligning within a half period timescale of the previously measured mid infrared photometric period of 85.8 ± 0.32 minutes. We attribute the emission to the electron cyclotron maser emission (ECME) and constrain the magnetic field strength to $B \gtrsim 1.4$ kG. We emphasise that the periods inferred are provisional considering the short observing durations. The combination of previously demonstrated atmospheric stability and newly detected radio emission in 2M2228 makes it a promising laboratory for testing magnetospheric currents-driven auroral models. Future coordinated James Webb Space Telescope (JWST) and radio observations will further probe the link between auroral activity and atmospheric dynamics in this brown dwarf.

Key words: stars: brown dwarfs – stars: magnetic field – radio continuum: stars

1 INTRODUCTION

After the first undisputed discovery of Gliese 229B, a brown dwarf of spectral type T (Nakajima et al. 1995; Oppenheimer et al. 1995), the catalogue of brown dwarfs was substantially enhanced using the 2-Micron All-Sky Survey (2MASS; Skrutskie et al. 2006; Kirkpatrick et al. 1999, 2000) largely due to improvement in infrared telescopic equipment. This development prompted the definition of new classes of substellar objects denoted L and T dwarfs at effective temperatures ranging between $T_{\text{eff}} \sim 2500$ –1300 K for L dwarfs and $T_{\text{eff}} \sim 1500$ –750 K for T dwarfs (Kirkpatrick 2005). Following the launch of the Wide-field Infrared Survey Explorer (WISE) telescope in 2009 and a subsequent full sky survey (Wright et al.

2010) a new class of substellar objects at $T_{\text{eff}} \lesssim 500$ K (Cushing et al. 2011) were detected and classified as Y dwarfs. These discoveries expanded our understanding of the low-temperature end of the substellar population, including brown dwarfs which are intermediate objects between planets and stars. Although no sharp boundary exists between giant planets and brown dwarfs, a common criterion for separating the two is the minimum mass required for deuterium fusion, with objects roughly above 13 Jupiter masses classified as brown dwarfs (Spiegel et al. 2011). The situation becomes more nuanced with the discovery of planetary mass objects with masses below the deuterium burning limit e.g. the free floating object in the star-forming cluster IC 348 at 3–4 M_J (Luhman et al. 2024). Because they cannot fuse deuterium, these objects are not considered brown dwarfs, although they share other physical and spectral properties with low-mass brown dwarfs. A new spectral class ‘H’ has now

* E-mail: kelvin.wandia@manchester.ac.uk

been proposed to account for such objects (Luhman & de Oliveira 2025). Conversely, brown dwarfs are separated from stars based on the mass limit of $\sim 0.075 M_{\odot}$ ($78.5 M_J$) required to ignite and sustain hydrogen fusion (Chabrier et al. 2023). While all T and Y dwarfs are generally brown dwarfs, young gas giant exoplanets can temporarily reach similar temperatures. Conversely, some early type L dwarfs are very low-mass stars, and some late type M dwarfs can be brown dwarfs. Objects of spectral type $>L2.5$ are generally believed to be brown dwarfs (Dieterich et al. 2014). Brown dwarfs together with very low-mass stars of spectral type later than $\sim M7V$ ($T_{\text{eff}} \lesssim 2700$ K) are collectively known as ultra cool dwarfs (UCDs; Cushing et al. 2006) and are expected to be fully convective.

Due to their convective interiors, UCDs are now known to be capable of supporting strong magnetic fields which have been attributed to an α^2 type dynamo at work in their interior (Chabrier & Küker 2006; Dobler et al. 2006; Browning 2008). These magnetic fields drive activity that may be observed at the surfaces of earlier-type UCDs, but is largely absent in later types due to their increasingly neutral atmospheres. In addition to their magnetic properties, the cooler temperatures of later-type UCDs allow their atmospheres to form and sustain complex molecules. Observations of their atmospheres in the mid infrared show photometric variabilities modulated by the rotation period caused by atmospheric heterogeneities and suggest the presence of complex weather patterns (e.g. Metchev et al. 2015; Buenzli et al. 2012; Yang et al. 2016).

One of the mechanisms through which UCDs generate radio emission is through the electron cyclotron maser emission (ECME; Wu & Lee 1979; Dulk 1985; Melrose & Dulk 1982; Callingham et al. 2024). ECME is a coherent emission mechanism arising from non-thermal anisotropic electrons in a horseshoe or a loss cone distribution (Melrose 2017). As a coherent emission mechanism, ECME can generate extremely high brightness temperatures which can exceed the 10^{12} K inverse Compton limit that applies to incoherent synchrotron emission (Kellermann & Pauliny-Toth 1969). The resulting radio emission is often highly circularly polarised emission, frequently approaching 100%, with detections of both helicities interpreted as arising from magnetic distinct regions and or changing magnetic field orientations with respect to the viewing angle (Williams 2018). The radio emission is also often rotationally modulated, reflecting the periodic visibility of the emitting regions (Hallinan et al. 2006; Williams 2018). The mechanism driving coherent radio emission in UCDs is believed to be analogous to that of the Jovian system involving large scale magnetospheric currents (Hallinan et al. 2015) caused by co-rotation breakdown primarily due to mass loading either from orbiting planets/moons or the interstellar medium (Nichols et al. 2012). Hallinan et al. (2015) have also proposed that magnetospheric currents are likely to contribute to observed photometric variability that traces weather in brown dwarfs.

Although radio activity is now beginning to be characterised in UCDs, the first detection of a brown dwarf at radio wavelengths by Berger et al. (2001) challenged standard theories of dynamo processes, activity, and temperature relationships. According to the temperature activity relationship, a hot chromosphere at a temperature of $\sim 10^4$ K and the coronal at a temperature of $\sim 10^7$ K emit H α and soft X-rays, respectively. The two act as tracers of magnetic activity. As such, the detection of strong magnetic fields in brown dwarfs, which do not appear to have a classic chromosphere and corona, came as a surprise. In addition, this detection violated the empirically derived Gudel-Benz relationship, which relates the X-ray fluxes from the corona to the 5 GHz radio emission (Guedel & Benz 1993). Subsequent detections of UCDs have been made at radio wavelengths (e.g. Berger 2002, 2006; Berger et al. 2009; Burgasser & Putman 2005;

Burgasser et al. 2013; Hallinan et al. 2007, 2008, 2015; McLean et al. 2011, 2012; Gizis et al. 2013, 2016; Lynch et al. 2016; Vedantham et al. 2020b; Rose et al. 2023) and have expanded our understanding of magnetic/radio activity in low-mass stars and substellar objects.

The coolest brown dwarfs detected at radio wavelengths are of spectral type T with seven confirmed detections. They include the T6/T6.5 WISEP J112254.73+255021.5 (Route & Wolszczan 2016; Williams et al. 2017), T6/T6.5.5 2MASS 10475385+2124234 (Route & Wolszczan 2012; Williams et al. 2013; Williams & Berger 2015), T2.5 SIMP J01365663+0933473 and T6/T6.5.5 2MASS J12373919+6526148 (Kao et al. 2016, 2018), T6/T6.5 BDR J1750+3809 (Vedantham et al. 2020a), T7.0+T5.5 binary WISEP J101905.63+652954.2 (Vedantham et al. 2023) and the T8 WISE J062309.94–045624.6 (Rose et al. 2023). These detections reveal that ultra-cool, low mass objects can host strong magnetic fields and support auroral processes, highlighting a continuum between stellar and planetary magnetism. While radio emission has not yet been detected from the coolest brown dwarfs, the Y dwarfs, observational constraints have been placed providing important limits on their magnetic activity (Kao et al. 2019). We note that the ultimate goal is the detection of magnetic fields from exoplanets, a prospect that may be realised with the upgraded Low Frequency Array (LOFAR 2.0) and the low frequency component of the Square Kilometre Array (SKA-low).

In response to the paucity of T dwarfs detected at radio wavelengths, we conducted a search of archival National Science Foundation Karl G. Jansky Very Large Array (VLA) data sets for observations targeting T-type brown dwarfs. We discovered unpublished (to the best of our knowledge) observations of the T6/T6.5 brown dwarf 2MASS J22282889-4310262. These observations aimed to extend the sample of the coldest brown dwarfs detected at radio wavelengths. In this manuscript, we describe the targets in Section 2, in Section 3 we outline the methodology used for the data analysis, in Section 4 we present our results and discussion, and finally, we summarise our findings in Section 5.

2 2MASS J22282889-4310262

The brown dwarf 2MASS J22282889-4310262 (hereinafter 2M2228) was first reported by Burgasser et al. (2003) and assigned the spectral class T6.5 but further re-classified as a T6 (Burgasser et al. 2006) and is at a distance of $\sim 10.64 \pm 0.79$ pc (Faherty et al. 2012). We note that both spectral types have been cited in the literature, depending on the reference used. 2M2228 is rapidly rotating at a photometric period of 1.43 ± 0.16 hours (Clarke et al. 2008). The rotation period makes it one of the most rapidly rotating known UCD of spectral type T (Tannock et al. 2021; Vos et al. 2022).

2M2228 has a peak-to-peak photometric variability of 15.4 ± 1.4 milli-magnitude (mmag) in the J-band (1.0 – $1.25 \mu\text{m}$) (Clarke et al. 2008). The atmosphere of the brown dwarf has been characterised using the Hubble Space Telescope (HST) Wide Field Camera 3 (WFC3) at 1.1 – $1.7 \mu\text{m}$ and the Spitzer Infrared Array Camera (IRAC) at $4.5 \mu\text{m}$ (Buenzli et al. 2012), which revealed vertical heterogeneities inferred from the phase shifts of light curves observed at the two wavelengths. Follow-up observations by Yang et al. (2016) found that the phase shifts between HST and Spitzer reported four years earlier by Buenzli et al. (2012) persisted, despite the measurements being separated by thousands of rotations, highlighting that the dwarf possesses long-lived vertical atmospheric structures. .

Property	Value	Reference
Spectral type	T6/T6.5	1
Distance (pc)	10.64 ± 0.79	2
T_{eff} (K)	900	3
J-band amplitude (mmag)	15.4 ± 1.4	4
Period (hrs)	1.43 ± 0.16	4
Radius (R_J)	0.94 ± 0.16	5
Age (Myr)	1000	5

Table 1. Physical parameters References:¹Burgasser et al. (2003, 2006),
²Faherty et al. (2012),³Buenzli et al. (2012),⁴Clarke et al. (2008),⁵Vos et al. (2020),

3 METHODS

3.1 Observations

We used archival observations (project code 15A-045, PI Aaron Golden) of 2M2228 conducted between 29-05-2015 and 31-05-2015 at C band (4–8 GHz) over two separate epochs on the aforementioned dates. The low declination of the source ($\sim -43^\circ$) required observations using the hybrid BnA configuration. The first epoch spanned 2 hours from 11:31 UTC to 13:31 UTC, and the second spanned a similar time frame from 11:16 UTC to 13:16 UTC, with the target observation beginning at 11:47 UTC for the first epoch and at 11:33 UTC for the second. Three sources were observed, 3C48 as the flux density calibrator, J2257-3657 as the phase calibrator, and 2M2228. The on-target time for each epoch was ~ 96 minutes, yielding a total time of ~ 192 minutes. The data from the observations were processed using the WIDAR correlator and recorded at 2 seconds of integration and 64 channels over 32 spectral windows (spws) each 128 MHz in size.

3.2 Calibration and Imaging

We processed the data using the VLA pipeline 6.6.1¹ which is based on the Common Astronomy Software Applications (CASA; CASA Team et al. 2022). The pipeline provided a series of automated recipes that flag, calibrate and image the data. Firstly, the data were exported from the VLA’s standard archival format, a Science Data Model-Binary Data Format (SDM-SDF) file, to a measurement set. The measurement set was then Hanning smoothed to reduce Gibbs ringing, flagged, and then flux density scaled using a standard flux calibrator (3C48 for these data). Various calibration steps were then performed, including correcting for the gain curves, opacities, antenna position errors, requantisation biases, switched and system power corrections and finally delay and bandpass calibrations. Calibration tables generated during each of the steps were applied to the data. Additional flagging was performed, and science-ready calibrated visibilities were obtained.

To diagnose the quality of the calibration, we produced un-deconvolved images for each individual observing epoch of both datasets using the CASA task `tclean`. We employed the multi-term multi-frequency (MTMFS; Rau & Cornwell 2011) algorithm to account for the large observing bandwidth (4 GHz). The images were Briggs weighted with a robust parameter of 0.5 (Briggs 1995). The theoretical Stokes I thermal noise for 2M2228 in a dual polarisation

Briggs weighted image at the robust parameter for each observation epoch was $\sim 2.3 \mu\text{Jy beam}^{-1}$. Finally, we performed deep deconvolution for both Stokes parameters using `tclean` to suppress the sidelobes. We used the `auto-multithresh` algorithm (Kepley et al. 2020), which is implemented in CASA, to perform automatic masking of emission during CLEAN (Högbom 1974; Clark 1980). We note that the Stokes V images are expected to be largely free of sidelobes as background radio sources, which are responsible for the sidelobes in the Stokes I, have low circular polarisation levels at $< 1\%$ (e.g. Macquart et al. 2003).

3.3 Astrometry

The pointing centre of the array during the observations did not account for the proper motion of 2M2228. We used the All Wide-field Infrared Survey Explorer (AllWISE) catalogue (Cutri et al. 2021), a reprocessing of WISE (Wright et al. 2010) and identified the source at coordinates 22h28m29.0153s and $-43^\circ 10m29.8312s$ in Right Ascension (RA) and Declination (Dec) respectively, at epoch 2010-07-23 (MJD 55400.0). The corresponding proper motions for the source are $102.3 \pm 5.8 \text{ mas yr}^{-1}$ and $-324.4 \pm 5.1 \text{ mas yr}^{-1}$ in RA and Dec (Faherty et al. 2012).

3.4 Radio Light Curves

To produce radio light curves, we closely followed the strategy of (Wandia et al. 2025) and employed `WSClean` (Offringa et al. 2014) to make a sky model by masking the target and deconvolving all other sources within the primary beam of the array. We then used the CASA task `ft` to add the modelled sources to the `modeldatacolumn` of the measurement set. The model was then subtracted from the visibilities using the task `uvsub` and the data phase shifted using the task `phaseshift` to the proper motion-corrected position of the target. We then accessed the visibilities stored in a measurement set using the `table` and `ms` tools available from the CASA toolkit `casatools`. Using these tools, we extracted and averaged the real parts of the visibilities over all baselines, channels and spectral windows for the parallel-hand correlations, RR and LL. We then binned the visibilities at a cadence of two minutes. Next, we computed the Stokes I and V as the sum and difference of RR and LL, respectively. We noted that flux scaling calibrators have associated errors due to difficulties in determining the true flux density. For C-band observations using 3C48 (0137+3309) for flux scaling, the error associated with the absolute flux density was $\sim 10\%$ ². To estimate the 1σ uncertainties, we added the scaling error in quadrature with a thermal noise of $\sim 16.7 \mu\text{Jy beam}^{-1}$ associated with a binning cadence of 2 minutes. We also produced dynamic spectra by binning the visibilities of the phase centered, background subtracted source at a cadence equal to the integration time. The light curves and dynamic spectra were validated through comparison with results obtained using `DSTOOLS`³, a radio data processing tool that extracts and plots light curves and dynamic spectra from radio interferometer visibilities.

¹ <https://science.nrao.edu/facilities/vla/data-processing/pipeline>

² https://www.vla.nrao.edu/astro/calib/vlacal/cal_mon/last/0137+3309.html

³ <https://github.com/askap-vast/dstools/tree/1e227ea26d1f6aed00afe56447ccbc61eae37a>

Epoch	Stokes	Peak Flux Density ($\mu\text{Jy beam}^{-1}$)
1	I	$67.3 \pm 4.9 \mu\text{Jy beam}^{-1}$
	V	$14.4 \pm 3.0 \mu\text{Jy beam}^{-1}$
2	I	$107.2 \pm 5.2 \mu\text{Jy beam}^{-1}$
	V	$-20.7 \pm 1.2 \mu\text{Jy beam}^{-1}$

Table 2. A summary of the measured Stokes I and V peak flux densities for each observing epoch.

4 RESULTS AND DISCUSSION

Emission from 2M2228 is detected in Stokes I and V from both observing epochs. The flux densities were extracted from the images by fitting a Gaussian profile using the CASA tool `imfit` and are presented in Table 2. The corresponding synthesised images reporting the detections are presented in Figure 1. The emission peak is found at coordinates 22h28m29.0690s -43d10m30.8146s in the first epoch and at coordinates 22h28m29.0831s -43d10m31.1885s in the second epoch. Close examination of the peak positions of the emission shows a positional shift of ~ 405 mas between the two observing epochs which is within the synthesised beam of $0.7''$. From the Stokes V measurements, the flux density changes sign from positive to negative between the two epochs, appearing to indicate a reversal in the line-of-sight component of the magnetic field at the emitter as opposite poles rotate into view. We note the source appears resolved in the Stokes I images. The current data are insufficient to determine the cause. We will explore this further with future, higher sensitivity observations.

4.1 Temporal Variability

The light curves for 2M2228 presented in Figure 2 (a) and (b) for the Stokes I and V reveal the source is displaying temporal variability. In Table 3 we present a summary of the timing, peak flux densities and their associated errors and fractional polarisation fractions of detected bursts. We note that all timestamps have been rounded to the nearest minute. Additionally, we present the fractional polarisation fractions in Figure 2 corresponding to each binned cadence for epochs one and two. Unfortunately, none of the bursts are captured in the dynamic spectra; consequently, the corresponding spectra are not presented.

We observe that in the bursts occur at an interval of ~ 47 minutes in the first epoch and ~ 58 minutes in the second. Considering 2M2228 has a half period 42.9 ± 4.8 minutes (Clarke et al. 2008), our analysis indicates the burst in the first epoch align within a half period timescale while the burst observed in the second epoch does not. We caution that the reported radio periodicities are tentative and precise periods can only be reliably determined through longer observations.

4.2 Emission Mechanism

To characterise the radio emission, we first evaluate the brightness temperatures T_B using equation 1

$$T_B \simeq \frac{S_\nu}{1 \mu\text{Jy}} \times \left(\frac{\nu}{1 \text{GHz}} \right)^{-2} \times \left(\frac{d}{1 \text{pc}} \right)^2 \times \left(\frac{L}{1 \text{cm}} \right)^{-2} \times 10^{26} \text{ K}, \quad (1)$$

where S_ν is the flux density in $\mu\text{Jy beam}^{-1}$, ν is the central frequency of the observation (6 GHz), d is the distance to the source

Epoch	Burst	Stokes	Peak Flux Density ($\mu\text{Jy beam}^{-1}$)	Time (UTC)	f_c (%)
1	1	I	380.8 ± 18.3	12:15	51.5 ± 5.0
		V	196.3 ± 16.7	12:15	
	2	I	290.7 ± 20.0	13:02	57.2 ± 7.0
		V	-166.2 ± 16.7	13:02	
2	1	I	330.8 ± 18.3	12:04	88.0 ± 7.0
		V	-291.1 ± 16.7	12:04	
	2	I	316.1 ± 20.0	13:02	84.2 ± 7.5
		V	-266.1 ± 16.7	13:02	

Table 3. A summary of the bursts observed from the light curve.

in parsec, and L is the size of the emitting region in cm. Assuming the source size is on the order of the radius of 2M2228, that is, $L \sim 0.94 R_J$ where $R_J = 7 \times 10^9$ cm is the Jovian radius, we determine $T_B \sim (4.9 - 7.8) \times 10^8$ K for peak flux densities measured from the images made using time and frequency averaged Stokes I visibilities in epoch one and two, respectively. We infer isotropic equivalent spectral luminosities $L_\nu = 4\pi d^2 S_\nu$ of $L_\nu \sim (9.1 - 14.5) \times 10^{12} \text{ erg s}^{-1} \text{Hz}^{-1}$ and radio luminosities $L_R = \int L_\nu d\nu \sim (3.65 - 5.81) \times 10^{22} \text{ erg s}^{-1}$ for the first and second epochs, respectively over an observing bandwidth $d\nu$.

To estimate the spectral indices, we divide the 4 GHz bandwidth into two equal sub-bands, each 2 GHz in size. We then make images for each sub-band and measure the integrated flux. We estimate the spectral index ($S \propto \nu^\alpha$) α at -2.56 ± 0.61 and -1.65 ± 0.40 for the first and second epoch respectively. The steep spectral indices for the first epoch may indicate a cut-off frequency where the flux density rapidly diminishes and the source becomes undetectable.

Besides plasma emission, the electron cyclotron maser emission (ECME) has been shown to be the dominant mechanism for the generation of coherent radio emission in low mass stars and brown dwarfs at cm wavelengths (Hallinan et al. 2007, 2008). ECME phenomenologically manifests as coherent, highly polarised bursts originating from spatially localised regions occurring at a local cyclotron frequency $\nu_c = 2.8 \times 10^6 B$ Hz, where B is the magnetic field strength in gauss, and exhibits a cut-off in frequency. Accordingly, we attribute the highly polarised emission observed in the light curves, which reaches $f_c \sim 100\%$ to ECME, and constrain the magnetic field strength of 2M2228 to $B \gtrsim 1.4$ kG.

5 SUMMARY AND FUTURE WORK

We have analysed archival VLA C band (4-8 GHz) band observations of the rapidly rotating T6/T6.5 brown dwarf 2MASS J22282889-4310262 (2M2228) over two observing epochs (2×96 minutes) and detected bursts occurring at intervals of ~ 47 and ~ 58 minutes respectively. This detection makes 2M2228 the eighth and notably, the most rapidly rotating T dwarf detected at radio wavelengths. From our Stokes I images, we have estimated brightness temperatures and inferred isotropic equivalent spectral luminosities of $L_\nu \sim 10^{12} \text{ erg s}^{-1} \text{Hz}^{-1}$ and radio luminosities of $L_R \sim 10^{22} \text{ erg s}^{-1}$. The large fractional polarisation ratios measured, $f_c > 50\%$, from the bursts suggest the emission is produced through the electron cyclotron maser emission (ECME) allowing us to constrain the magnetic field strength of 2M2228 to $B \gtrsim 1.4$ kilogauss. We caution that the inferred periodicities are provisional considering the brief observation durations.

The VLA detection of periodic, highly polarised radio bursts from

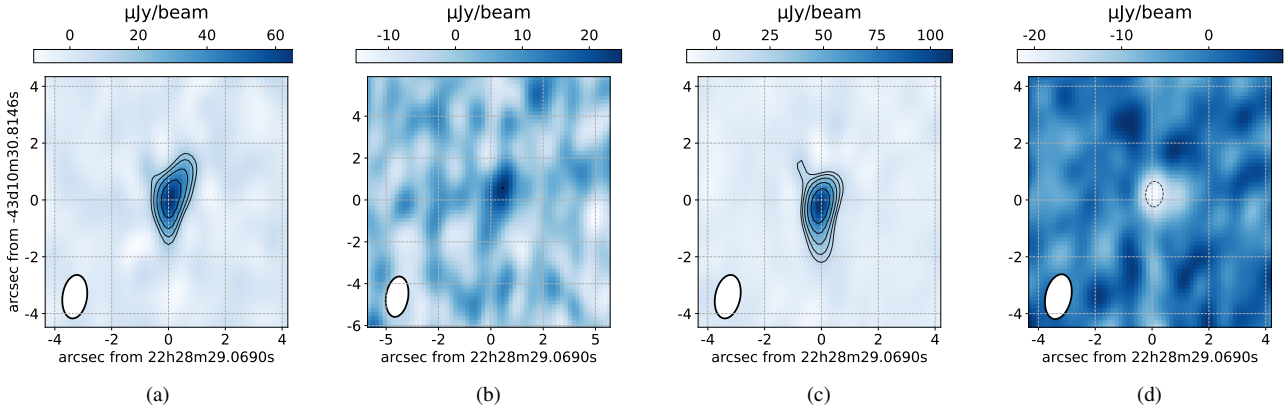


Figure 1. Stokes I and V images of 2M2228 for the observations conducted over two epochs. Panels (a) and (b) correspond to observations of the first epoch, and panels (c) and (d) to epoch two observations. (a) The source is detected in the Stokes I at a peak flux density $67.3 \pm 4.9 \mu\text{Jy beam}^{-1}$. The 1σ r.m.s. noise in the image is $3.1 \mu\text{Jy beam}^{-1}$ resulting in a signal to noise ratio (SNR) ~ 22 . (b) The corresponding Stokes V image is detected at a peak flux density $14.4 \pm 3.0 \mu\text{Jy beam}^{-1}$ at a 1σ r.m.s noise of $3.3 \mu\text{Jy beam}^{-1}$ giving a SNR ~ 4 . (c) Stokes I image for the second observing epoch. The detection is at a peak flux density $107.2 \pm 5.2 \mu\text{Jy beam}^{-1}$ at a 1σ r.m.s noise of $3.9 \mu\text{Jy beam}^{-1}$ giving a SNR ~ 27 . (d) The corresponding Stokes V image for the observation. The detection is at a peak flux density $-20.7 \pm 1.2 \mu\text{Jy beam}^{-1}$ at a 1σ r.m.s noise of $3.5 \mu\text{Jy beam}^{-1}$ giving a SNR ~ 6 . The peak flux is negative, indicating the left-hand circular polarisation is dominant. All the contours are drawn at $5\sigma \times (-4, -2\sqrt{2}, -2, -\sqrt{2}, -1, 1)$. In all the images, positive contours are represented by the solid line and negative contours by the broken line. The white ellipse with a black outline to the bottom left of the image represents the synthesised beam. All the positions are with respect to the detected positions at the first epoch.

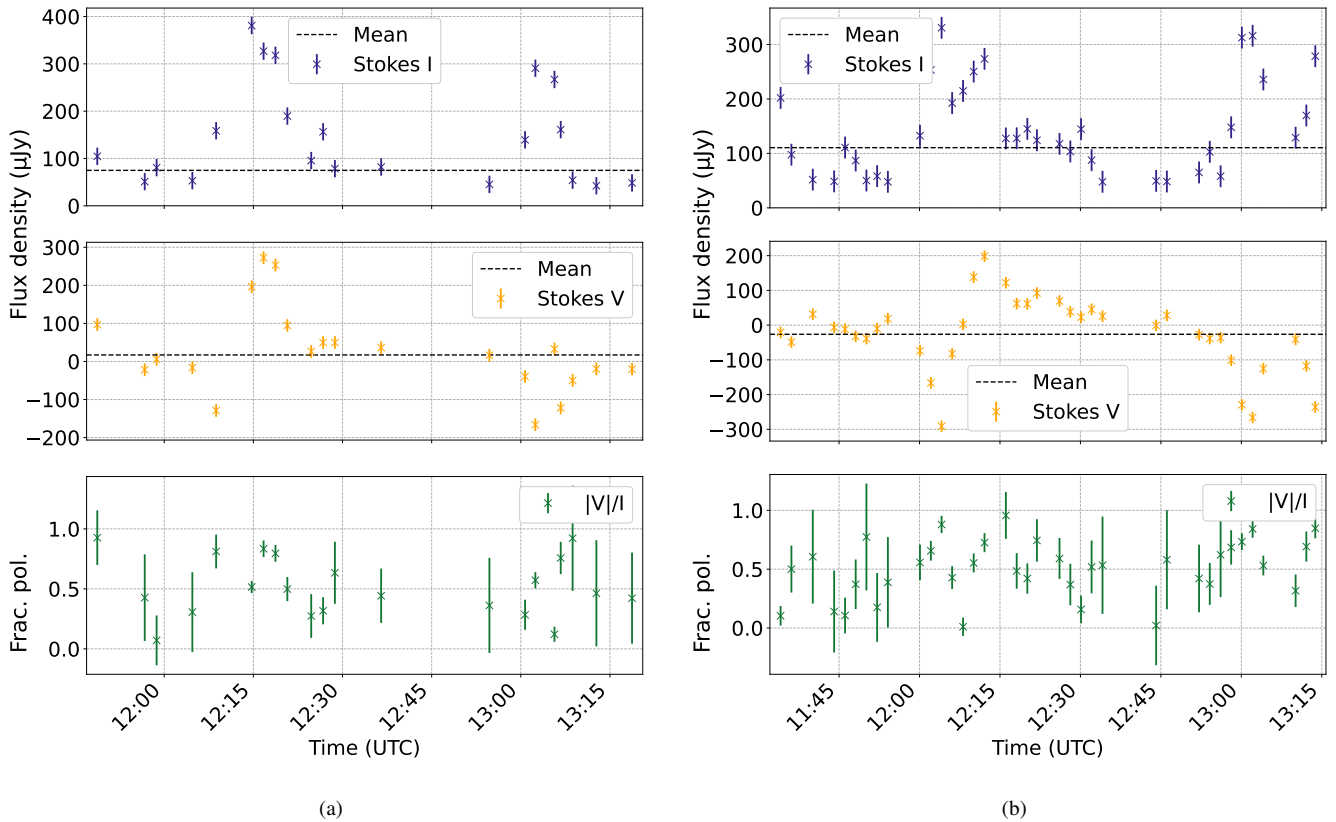


Figure 2. (a) Upper panel: Stokes I light curves for epoch one observations at 4-8 GHz with the data binned a cadence of 2 min. Center panel: the corresponding Stokes V light curve. The mean values for the Stokes I and V are $78.2 \mu\text{Jy beam}^{-1}$ and $11.0 \mu\text{Jy beam}^{-1}$. Lower panel: the fractional polarisation obtained as the ratio of the absolute Stokes V value to the Stokes I for each binned point. (b) Stokes I and V light curves for epoch two observations displayed using a similar panel layout to epoch one observations. The broken line represents the mean flux density. The mean values for the Stokes I and V are $122.1 \mu\text{Jy beam}^{-1}$ and $-27.3 \mu\text{Jy beam}^{-1}$. Lower panel: the fractional polarization fraction obtained as the ratio of the absolute Stokes V value to the Stokes I for each binned point. The light curves were filtered to remove unphysical values, specifically cases with fractional polarization greater than 1 and data points with excessively large errors.

2M2228, combined with the demonstrated long-term stability of its atmospheric structure (Yang et al. 2016), makes this brown dwarf an excellent target for coordinated multi-wavelength observation. Joint radio and James Webb Space Telescope (JWST) monitoring could provide complementary insights, enhancing the prospects of detecting sustained auroral emission. The persistence of the phase shifted between different wavelengths in the mid infrared light curves over thousands of rotations indicates that the underlying atmospheric structure maybe stable on multi-year timescales, increasing the likelihood that auroral phenomena are sustained rather than transient. JWST’s unprecedented sensitivity and spectral resolutions in the near and mid infrared may enable the detection of faint auroral tracers such as H₃⁺ that were previously inaccessible to other facilities (Gibbs & Fitzgerald 2022; Pineda et al. 2024). Moreover, its ability to perform time-resolved spectroscopy could distinguish auroral emission from associated weather phenomena through its characteristic spectral signatures. Recent work has demonstrated the instruments ability to map atmospheric features in the planetary mass radio loud T dwarf SIMP J0136+0933 (McCarthy et al. 2025), highlighting the potential for infrared auroral emission to contribute to complex atmospheric features.

Together, the combination of atmospheric stability and detected radio emission makes 2M2228 a particularly promising laboratory for testing the framework proposed by Hallinan et al. (2015), in which large magnetospheric currents drive multi-wavelength aurorae and influence atmospheric weather. More generally such observations will advance our understanding of auroral processes and their connection to atmospheric dynamics in T-type brown dwarfs, which serve as analogs to many directly imaged gas giant planets.

ACKNOWLEDGEMENTS

This project has been made possible in part by a grant from the SETI Institute. This work made use of Astropy:3, a community-developed core Python package and an ecosystem of tools and resources for astronomy (Astropy Collaboration et al. 2013, 2018, 2022). The National Radio Astronomy Observatory is a facility of the National Science Foundation operated under cooperative agreement by Associated Universities, Inc. This research has made use of the SIMBAD database, operated at CDS, Strasbourg, France. This research has made use of the VizieR catalogue access tool, CDS, Strasbourg, France. This publication makes use of data products from the Wide-field Infrared Survey Explorer, which is a joint project of the University of California, Los Angeles, and the Jet Propulsion Laboratory/California Institute of Technology, funded by the National Aeronautics and Space Administration.

DATA AVAILABILITY

Data underlying this article are publicly available in the NRAO Data Archive at <https://data.nrao.edu/portal> and can be accessed with project code 15A-045.

REFERENCES

- Astropy Collaboration et al., 2013, *A&A*, **558**, A33
 Astropy Collaboration et al., 2018, *AJ*, **156**, 123
 Astropy Collaboration et al., 2022, *apj*, **935**, 167
 Berger E., 2002, *ApJ*, **572**, 503
 Berger E., 2006, *ApJ*, **648**, 629
 Berger E., et al., 2001, *Nature*, **410**, 338
 Berger E., et al., 2009, *ApJ*, **695**, 310
 Briggs D. S., 1995, in American Astronomical Society Meeting Abstracts p. 112.02
 Browning M. K., 2008, *ApJ*, **676**, 1262
 Buenzli E., et al., 2012, *ApJ*, **760**, L31
 Burgasser A. J., Putman M. E., 2005, *ApJ*, **626**, 486
 Burgasser A. J., McElwain M. W., Kirkpatrick J. D., 2003, *AJ*, **126**, 2487
 Burgasser A. J., Burrows A., Kirkpatrick J. D., 2006, *ApJ*, **639**, 1095
 Burgasser A. J., Melis C., Zauderer B. A., Berger E., 2013, *ApJ*, **762**, L3
 CASA Team et al., 2022, *PASP*, **134**, 114501
 Callingham J. R., et al., 2024, arXiv e-prints, p. arXiv:2409.15507
 Chabrier G., Küker M., 2006, *A&A*, **446**, 1027
 Chabrier G., Baraffe I., Phillips M., Debras F., 2023, *A&A*, **671**, A119
 Clark B. G., 1980, *A&A*, **89**, 377
 Clarke F. J., Hodgkin S. T., Oppenheimer B. R., Robertson J., Haubois X., 2008, *MNRAS*, **386**, 2009
 Cushing M. C., et al., 2006, *ApJ*, **648**, 614
 Cushing M. C., et al., 2011, *ApJ*, **743**, 50
 Cutri R. M., et al., 2021, VizieR Online Data Catalog: AllWISE Data Release (Cutri+ 2013), VizieR On-line Data Catalog: II/328. Originally published in: IPAC/Caltech (2013)
 Dieterich S. B., Henry T. J., Jao W.-C., Winters J. G., Hosey A. D., Riedel A. R., Subasavage J. P., 2014, *AJ*, **147**, 94
 Dobler W., Stix M., Brandenburg A., 2006, *ApJ*, **638**, 336
 Dulk G. A., 1985, *ARA&A*, **23**, 169
 Faherty J. K., et al., 2012, *ApJ*, **752**, 56
 Gibbs A., Fitzgerald M. P., 2022, *AJ*, **164**, 63
 Gizis J. E., Burgasser A. J., Berger E., Williams P. K. G., Vrba F. J., Cruz K. L., Metchev S., 2013, *ApJ*, **779**, 172
 Gizis J. E., et al., 2016, *AJ*, **152**, 123
 Guedel M., Benz A. O., 1993, *ApJ*, **405**, L63
 Hallinan G., Antonova A., Doyle J. G., Bourke S., Brisken W. F., Golden A., 2006, *ApJ*, **653**, 690
 Hallinan G., et al., 2007, *ApJ*, **663**, L25
 Hallinan G., Antonova A., Doyle J. G., Bourke S., Lane C., Golden A., 2008, *ApJ*, **684**, 644
 Hallinan G., et al., 2015, *Nature*, **523**, 568
 Högbom J. A., 1974, *A&AS*, **15**, 417
 Kao M. M., Hallinan G., Pineda J. S., Escala I., Burgasser A., Bourke S., Stevenson D., 2016, *ApJ*, **818**, 24
 Kao M. M., Hallinan G., Pineda J. S., Stevenson D., Burgasser A., 2018, *ApJS*, **237**, 25
 Kao M. M., Hallinan G., Pineda J. S., 2019, *MNRAS*, **487**, 1994
 Kellermann K. I., Pauliny-Toth I. I. K., 1969, *ApJ*, **155**, L71
 Kepley A. A., Tsutsumi T., Brogan C. L., Indebetouw R., Yoon I., Mason B., Donovan Meyer J., 2020, *PASP*, **132**, 024505
 Kirkpatrick J. D., 2005, *ARA&A*, **43**, 195
 Kirkpatrick J. D., et al., 1999, *ApJ*, **519**, 802
 Kirkpatrick J. D., et al., 2000, *AJ*, **120**, 447
 Luhman K. L., de Oliveira C. A., 2025, A New Spectral Class of Brown Dwarfs at the Bottom of the IMF in IC 348, doi:10.48550/ARXIV.2506.08969, <https://arxiv.org/abs/2506.08969>
 Luhman K. L., Alves de Oliveira C., Baraffe I., Chabrier G., Geballe T. R., Parker R. J., Pendleton Y. J., Tremblin P., 2024, *AJ*, **167**, 19
 Lynch C., Murphy T., Ravi V., Hobbs G., Lo K., Ward C., 2016, *MNRAS*, **457**, 1224
 Macquart J. P., Wu K., Sault R., Hannikainen D. C., 2003, in Durouchoux P., Fuchs Y., Rodriguez J., eds, New Views on Microquasars. p. 232 (arXiv:astro-ph/0111302), doi:10.48550/arXiv.astro-ph/0111302
 McCarthy A. M., et al., 2025, *The Astrophysical Journal Letters*, **981**, L22
 McLean M., Berger E., Irwin J., Forbrich J., Reiners A., 2011, *ApJ*, **741**, 27
 McLean M., Berger E., Reiners A., 2012, *ApJ*, **746**, 23
 Melrose D. B., 2017, *Reviews of Modern Plasma Physics*, **1**, 5
 Melrose D. B., Dulk G. A., 1982, *ApJ*, **259**, 844
 Metchev S. A., et al., 2015, *ApJ*, **799**, 154

- Nakajima T., Oppenheimer B. R., Kulkarni S. R., Golimowski D. A.,
Matthews K., Durrance S. T., 1995, [Nature](#), **378**, 463
- Nichols J. D., Burleigh M. R., Casewell S. L., Cowley S. W. H., Wynn G. A.,
Clarke J. T., West A. A., 2012, [ApJ](#), **760**, 59
- Offringa A. R., et al., 2014, [MNRAS](#), **444**, 606
- Oppenheimer B. R., Kulkarni S. R., Matthews K., Nakajima T., 1995, [Science](#),
270, 1478
- Pineda J. S., Hallinan G., Desert J.-M., Harding L. K., 2024, [ApJ](#), **966**, 58
- Rau U., Cornwell T. J., 2011, [A&A](#), **532**, A71
- Rose K., et al., 2023, [ApJ](#), **951**, L43
- Route M., Wolszczan A., 2012, [ApJ](#), **747**, L22
- Route M., Wolszczan A., 2016, [ApJ](#), **821**, L21
- Skrutskie M. F., et al., 2006, [AJ](#), **131**, 1163
- Spiegel D. S., Burrows A., Milsom J. A., 2011, [ApJ](#), **727**, 57
- Tannock M. E., et al., 2021, [AJ](#), **161**, 224
- Vedantham H. K., et al., 2020a, [Nature Astronomy](#), **4**, 577
- Vedantham H. K., et al., 2020b, [ApJ](#), **903**, L33
- Vedantham H. K., et al., 2023, [A&A](#), **675**, L6
- Vos J. M., et al., 2020, [AJ](#), **160**, 38
- Vos J. M., Faherty J. K., Gagné J., Marley M., Metchev S., Gizis J., Rice
E. L., Cruz K., 2022, [The Astrophysical Journal](#), **924**, 68
- Wandia K., et al., 2025, [MNRAS](#), **543**, 1935
- Williams P. K. G., 2018, in Deeg H. J., Belmonte J. A., eds, , Handbook of
Exoplanets. p. 171, doi:10.1007/978-3-319-55333-7_171
- Williams P. K. G., Berger E., 2015, [ApJ](#), **808**, 189
- Williams P. K. G., Berger E., Zauderer B. A., 2013, [ApJ](#), **767**, L30
- Williams P. K. G., Gizis J. E., Berger E., 2017, [ApJ](#), **834**, 117
- Wright E. L., et al., 2010, [AJ](#), **140**, 1868
- Wu C. S., Lee L. C., 1979, [ApJ](#), **230**, 621
- Yang H., et al., 2016, [ApJ](#), **826**, 8

This paper has been typeset from a $\text{\TeX}/\text{\LaTeX}$ file prepared by the author.